

Compact and Tunable Forward Coupler Based on High-Impedance Superconducting Nanowires


Marco Colangelo^{1,†}, Di Zhu^{1,2,†}, Daniel F. Santavicca³, Brenden A. Butters¹, Joshua C. Bienfang⁴, and Karl K. Berggren^{1,*}

¹*Research Laboratory of Electronics, Massachusetts Institute of Technology, Cambridge, Massachusetts 02139, USA*

²*John A. Paulson School of Engineering and Applied Science, Harvard University, Cambridge, Massachusetts 02138, USA*

³*Department of Physics, University of North Florida, Jacksonville, Florida 32224, USA*

⁴*National Institute of Standards and Technology, Gaithersburg, Maryland 20899, USA*

 (Received 8 November 2020; revised 19 January 2021; accepted 1 February 2021; published 25 February 2021)

Developing compact, low-dissipation, cryogenic-compatible microwave electronics is essential for scaling up low-temperature quantum computing systems. In this paper, we demonstrate an ultracompact microwave directional forward coupler based on high-impedance slow-wave superconducting-nanowire transmission lines. The coupling section of the fabricated device has a footprint of $416 \mu\text{m}^2$. At 4.753 GHz, the input signal couples equally to the through port and forward-coupling port (50:50) at -6.7 dB with -13.5 dB isolation. The coupling ratio can be controlled with dc bias current or temperature by exploiting the dependence of the kinetic inductance on these quantities. The material and fabrication processes are suitable for direct integration with superconducting circuits, providing a practical solution to the signal distribution bottlenecks in developing large-scale quantum computers.

DOI: [10.1103/PhysRevApplied.15.024064](https://doi.org/10.1103/PhysRevApplied.15.024064)

I. INTRODUCTION

The scalability of superconducting quantum systems is constrained by the distribution of microwave signals to the quantum processors [1]. Within current designs, each qubit is individually wired for readout and control [1,2], entailing an increasing number of devices and cables as the size of the circuit is increased. Inevitably, the present approach will lead to challenges in packaging, routing, thermalization, and footprint [3]. To realize large-scale circuits with thousands of qubits, most of the microwave electronics will need to be integrated on-chip [1,3], necessitating the development of miniaturized low-power, low-dissipation rf devices. More broadly, a small-footprint cryogenic microwave electronics platform is also required for the advancement of several other applications relying on processing electrical signals at low temperature, such as single-photon detection [4], superconducting quantum interference device magnetometry [5,6], and radio astronomy [7,8].

Many of the proposals to address scalability in superconducting circuits face several challenges in satisfying the requirements for on-chip integrability. Devices based

on semiconductors [9–13] either dissipate too much power to be operated at a few millikelvin [1] or are made from unconventional materials for which integration with superconductors has not yet been demonstrated. Among the superconducting solutions, 50Ω transmission-line-based devices [14–16] require too large a footprint for large-scale integration. Josephson junction (JJ) electronics are a natural candidate for integration with JJ-based quantum processors [17–22], but they can be challenging to manufacture and require magnetic shielding.

Recently, superconducting nanowires have emerged as an alternative approach to realize ultracompact microwave devices [23,24]. The high kinetic inductivity achieved with disordered superconducting thin films provides an effective means of realizing extremely high characteristic-impedance transmission lines with zero dc resistance, minimal microwave dissipation, slow phase velocity (high effective refractive index), and very small footprint. The native high-impedance, high-index operation generates electromagnetically protected microwave environments that could well interface to superinductor-based qubits [25–28]. The compatibility with these applications is enabled by the rather conventional materials and by the few-layer fabrication process [29,30], making the devices realized with superconducting nanowires a viable solution to the signal distribution bottlenecks of quantum computers.

*berggren@mit.edu

†These authors contributed equally to this work.

Conventional directional coupler modules split, combine, and distribute microwave fields to the subsequent processing layers or to the readout [15,31,32]. They carry out essential processing tasks but take up a significant volume inside the cryostat. Here, we use high kinetic-inductance superconductors to demonstrate a compact high-impedance directional coupler. Our miniaturized coupler is based on niobium nitride (NbN) superconducting nanowire side-coupled striplines embedded in a multilayer dielectric stack. In Fig. 1(a) we show optical and scanning electron micrographs of the fabricated device. We achieve forward coupling in the gigahertz range in an extremely reduced footprint and with impedance-matching flexibility. We further demonstrate that the nonlinear dependence of the nanowire's kinetic inductance on dc current and temperature allow the microwave properties of the coupler to be tuned. We suggest this device may find application in superconducting quantum computing systems and in other low-temperature applications where small-footprint on-chip tunable coupling at microwave frequency is needed.

II. DEVICE MODELING, DESIGN, AND FABRICATION

Our device is designed following a traditional coupled-line architecture [Fig. 1(b)] where two superconducting nanowires are brought together for a coupling length l . The structure can be modeled (Appendix A) as a coupled LC ladder [Fig. 1(b)(i)] using a standard coupled-mode formalism [33–35], with some modifications to capture the kinetic-inductive transmission line [36]. To reflect the high-inductivity behavior of nanowires, we explicitly separate the kinetic contribution (\mathcal{L}_k) from the geometric (Faraday) contribution (\mathcal{L}_F) to the total line inductance per unit length. The coupling produces mode splitting into common (c) and differential (π) modes, with different effective indices and propagation constants (β_c and β_π). In a transmission line, a sinusoidal signal with frequency ω is a superposition of these eigenmodes and energy is continuously transferred between the two lines with a periodicity $l_\pi = \pi/\Delta\beta = \pi/(\beta_\pi - \beta_c)$. A section of coupled transmission line with a length that is an odd-integer multiple of

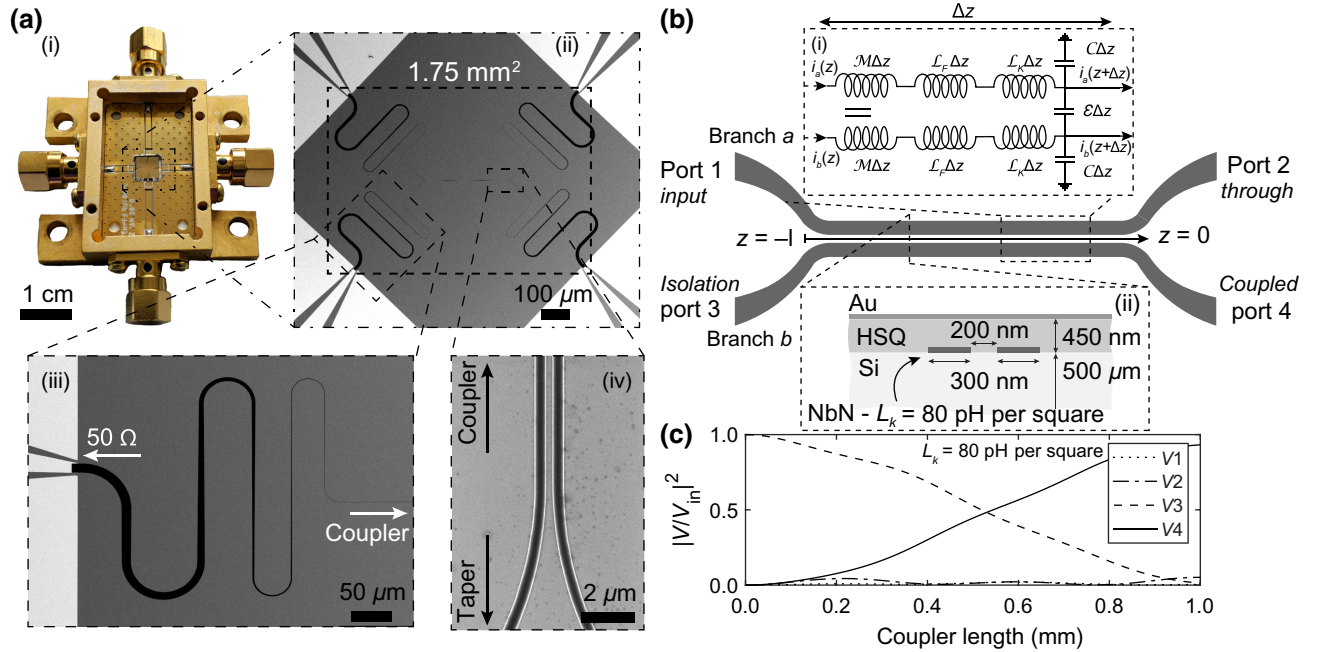


FIG. 1. Superconducting-nanowire directional forward coupler: device and model. (a) Optical and scanning electron micrographs (SEMs) of the fabricated device: (i) device die mounted in the radio-frequency (rf) testing box; (ii) SEM showing the full four-port device before the fabrication of the dielectric spacer and the top ground; (iii) closeup SEM of the impedance-matching taper; (iv) closeup SEM of the coupled nanowire transmission lines. (b) Geometry, model, and implementation of coupler: two nanowire transmission lines brought together for a coupling length l . (i) Analytical model: coupled LC ladder, where we explicitly separated the geometric (Faraday) component of the total line inductance per unit length (p.u.l.), \mathcal{L}_F , from the kinetic inductance p.u.l. \mathcal{L}_k ; C is the capacitance p.u.l. of each line; \mathcal{E} is the coupling capacitance p.u.l.; \mathcal{M} is the mutual inductance p.u.l. (ii) Implementation as side-coupled striplines. In the analytical model, the gold layers (Au) have been treated as perfect electric conductors. (c) Simulation of the port voltages versus coupler length at 5 GHz for 50:50 forward coupling ($L_k = 80$ pH per square).

$l_\pi/2$ can perform, in the ideal case, 3 dB forward coupling at ω . In rf transmission lines made of conventional materials, the splitting in propagation constant $\Delta\beta$ is relatively small and the minimum length required to achieve forward coupling (at a target frequency) is relatively large. Therefore, it is generally more convenient to exploit the difference in the characteristic impedance of the eigenmodes to realize low-coupling backward directional couplers [34,37]. With coupled superconducting nanowires, the combination of high-kinetic inductance lines, high coupling capacitance, and low loss boosts $\Delta\beta \propto \sqrt{\mathcal{L}_k \mathcal{C}} \sqrt{1 + 2\mathcal{E}/\mathcal{C}}$ and allows forward coupling in a small footprint (l_π is relatively small). Here, \mathcal{C} and \mathcal{E} are the self and coupling capacitance per unit length, respectively.

To practically illustrate this concept, we consider the side-coupled stripline implementation shown in Fig. 1(b)(ii), which we use to realize our device. The lines are made of a 300 nm wide, 7 nm thick NbN nanowire with a sheet kinetic inductivity of $L_k = 80$ pH per square, separated by a 200 nm wide gap. Here, NbN is selected for fabrication convenience. Alternative high-inductivity materials (e.g., granular aluminum [28]) can be used. The structures are patterned on silicon and referenced to a 60 nm top-side gold ground plane through a 450 nm thick hydrogen silsequioxane (HSQ) dielectric layer, with $\epsilon_r = 2.9$ [38,39]. In this microwave environment, the simulated characteristic impedance is $Z_0 = 1446 \Omega$ and the effective index $n_{\text{eff}} = 54.5$, which reduces the phase velocity to 1.8% of c and highly compresses the guided wavelength. In Appendix B we study the dependence of these parameters on the conductor width and its kinetic inductance. For clarity, the port naming convention is shown

in Fig. 1(b). In Fig. 1(c) we show that a 5 GHz signal injected through the input port of the coupling section takes $l_\pi/2 = \pi/(2\Delta\beta) = 539 \mu\text{m}$ to forward couple 50% of the power to the other branch. Compared to the same structure realized with conventional conductors [40], this coupling section achieves an almost 2 orders of magnitude footprint reduction (Fig. 4).

The device is fabricated with design parameters based on the modeling results. A rationale for our feature size range selection was to make the fabrication compatible with foundry processing to facilitate large-scale integration. For the realization of this prototype, the superconducting layer is patterned with electron beam lithography. Nevertheless, the minimum feature size complies with state-of-the-art deep UV photolithography resolution. See Appendix C for details on the fabrication process. In Fig. 1(a) we show micrographs of the device before the fabrication of the dielectric spacer and the top ground. In the final design we used a coupling length $l = 520 \mu\text{m}$ and we included four 2.5 GHz high-pass Klopfenstein impedance-matching tapers [Fig. 1(a)(iii)] [39,41–44]. Details on the design and characterization of the taper can be found in Appendix D. Coplanar waveguide (CPW) signal feed lines (60 nm gold) are also fabricated to allow wire bonding and packaging. The footprint of the full superconducting structure [as outlined in Fig. 1(a)(ii)] is 1.75 mm^2 , while the high-impedance coupling section only occupies $416 \mu\text{m}^2$.

The addition of the tapers, while increasing the total footprint of the device, improves flexibility, affording the possibility to interface the high-impedance coupling section to lower-impedance environments without

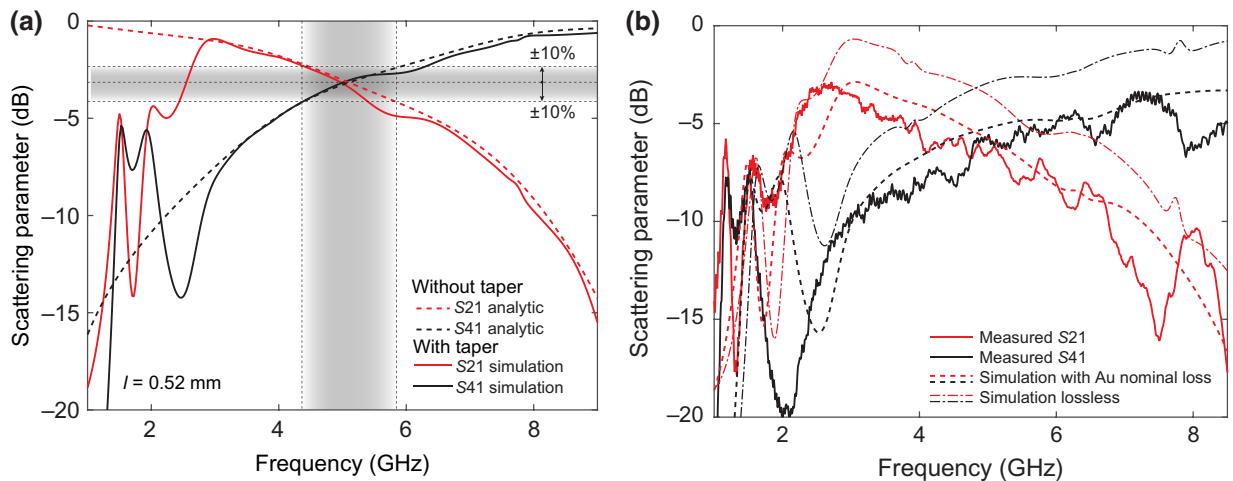


FIG. 2. Microwave response of the directional forward coupler. (a) Analytical modeling of the coupling section (without taper) and simulation of the impedance-matched coupler. Above 3 GHz the curves match, showing that the impedance-matching taper, interfacing the high-impedance coupling section to the 50Ω rf electronics, does not disturb the coupling operation. The 10% bandwidth is 4.4 to 5.8 GHz. (b) Measured microwave response of the fabricated device at 1.3 K. We compare the data to simulation, corrected for fabrication nonidealities, and including normal conductor losses from the Au ground plane and CPW feedlines. The balanced forward coupling is observed at 4.753 GHz.

disturbing the forward-coupling operation. In this case we interface the high-impedance nanowire transmission line coupler to $50\ \Omega$ rf electronics. In Fig. 2(a) we show that, in the taper passband ($f \geq 3$ GHz), the simulation results (full wave) of the impedance-matched coupler correctly reproduce the analytic calculation of the high-impedance coupling section response with minimal deviations. The 50% coupling point is at 4.99 GHz, with the isolation parameter at -21.9 dB. In the figure we also show the coupler operation bandwidth that we arbitrarily set for a ± 0.1 coupling ratio deviation (namely 60:40-40:60 coupling, 10% bandwidth). According to the analytic model, the coupler operation 10% bandwidth is 4.4 to 5.8 GHz. For the impedance-matched device, the in-band ripple of the Klopfenstein tapers (Fig. 6) shrinks the bandwidth. This can be improved by adopting alternative taper designs with minimal in-band ripple [45]. In general, symmetric single section 3 dB couplers are characterized by a relatively narrow bandwidth [40,46]. For wideband operation, designs based on asymmetric coupled lines [46] or hybrids [47] can be used. In Appendix E we discuss the bandwidth of parallel line couplers and we show an asymmetric design achieving wideband operation.

III. RESULTS AND DISCUSSION

We measure the microwave response of the fabricated coupler at 1.3 K with a vector network analyzer providing effective signal power lower than -60 dBm. In the same cooldown, we calibrate the cable and connector loss (cryostat to device box) to scale the measured data. In Fig. 2(b) we show that the forward-coupling behavior is observed. At 4.753 GHz, the input signal from port 1 couples equally to the through port (port 2) and forward-coupling port (port 4) with a level of -6.7 dB, and the isolation parameter $S_{31} = -13.5$ dB. The device is reciprocal (see the Supplemental Material [48]). For comparison, we show simulations of the impedance-matched coupler, including the response of the feed lines, and corrected to account for fabrication nonidealities. The slight discrepancy (approximately 500 MHz) between the measured and simulated coupling frequencies can be attributed to the uncertainties in the device parameters. For example, the fabrication process, consisting of several lithographic and etching steps, may induce a degradation of the film leading to an increase in the kinetic inductance that would explain this observation (Appendix C).

We attribute the inconsistency in the magnitude of the S parameters to device-level conductor losses contributing to most of the insertion loss of the coupler. In fact, the agreement with the simulation improves when we include normal conductor losses for the Au layers. This is also confirmed by the characterization of the Klopfenstein tapers for which the same discrepancies between simulation and measurements are observed (Fig. 6). We attribute

the additional loss to contributions that are not accounted for in the calibration. In this experiment, the calibration does not account for losses and reflection from the sample holder Printed Circuit Board (PCB), wire bonds, and structure transitions. Moreover, due to setup limitations, the reflection parameters cannot be measured.

The isolation parameter is at a significantly different level from the expected value. This discrepancy (approximately 8.5 dB) might be caused by factors such as the impedance-matching taper deviating from the prescribed design, with suboptimal impedance matching and additional backward reflections, and the specific full device simulation not including element-to-element transitions (e.g., abrupt transition from stripline to CPW). The intrinsic isolation performance of the coupler can be improved by reducing the difference between the characteristic impedance of the modes [36,40]. According to Eqs. (A23) and (A24), this can be achieved by tuning the capacitive terms of the system. See the Supplemental Material [48] for design parameters of the coupler with improved isolation performance.

The microwave response is characterized with effective injected currents much smaller than the device depairing current I_d . Assuming an ideal broadband impedance transformer, with perfect matching and transmission, $I_H = V_L / \sqrt{Z_L Z_H}$, where I_H is the current at the high impedance terminal and V_L is voltage applied at the low-impedance end [42]. For $Z_L = 50\ \Omega$ and $Z_H = 1446\ \Omega$, a -60 dBm signal converts to a $V_{pk,Z_L} = 316.2\ \mu\text{V}$ and $I_{pk,Z_H} = 1.2\ \mu\text{A}$. Here I_{pk,Z_H} is much lower than the switching current of the wire, and therefore of its depairing current. In this small-signal condition the device response is independent of the applied microwave power.

The kinetic inductance however strongly depends on carrier density, which can be tuned with current (I_b) and with temperature (T): $L_k = L_k(x' = I_b/I_{sw}, t = T/T_c)$, where I_{sw} is the switching current and T_c is the critical temperature. Leveraging these dependencies affords the possibility of dynamically modulating the microwave characteristics of the modes in the lines, creating active, tunable devices. When the bias current in the nanowire approaches the depairing current ($x = I_b/I_d \rightarrow 1$), the kinetic inductance diverges hyperbolically, $L_k(x) \propto (1 - x^\alpha)^{-1/\alpha}$ with α determined by the operating temperature of the device [52]. Because of fabrication imperfections, superconducting nanowire devices similar to those described in this paper can typically only reach a fraction of the depairing current, with the switching current $I_{sw} \approx 70\% I_d$ [53]. In Fig. 3(a) we show that with this assumption and given the measurement condition ($\alpha = 2.27$) [52], a 30% theoretical maximum increment of the kinetic inductance might be expected. In the coupled-line architecture the two nanowires are galvanically isolated. Hence, the kinetic inductance of each nanowire can be tuned independently. We characterize the device tunability

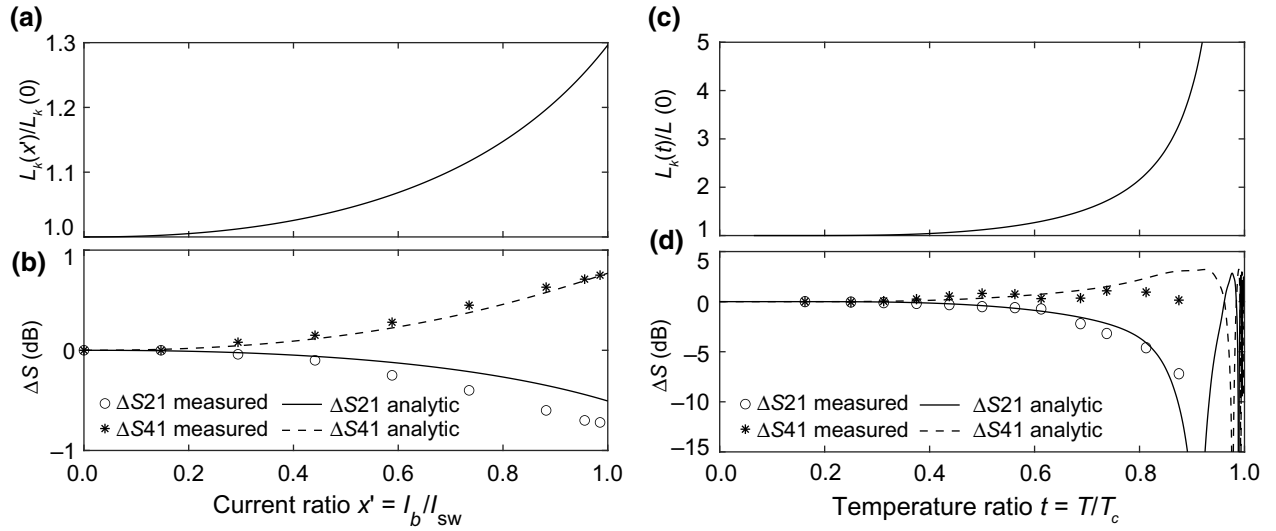


FIG. 3. Nonlinear dependence of the kinetic inductance $L_k(x' = I_b/I_{sw}, t = T/T_c)$ and coupler response tunability at = 4.75 GHz with bias current and temperature. (a) Kinetic inductance's dependence on current, for $I_{sw}/I_d = 0.7$, according to the fast relaxation model with $\alpha = 2.27$. (b) Tunability of the transmission (S21) and coupling (S41) responses as a function of the current (normalized by I_{sw}) supplied through the isolation port. The measured data (symbols) well match our analytical model (lines) based on a coupled-mode formulation with current-dependent kinetic inductance. (c) Kinetic inductance's dependence on temperature calculated from the explicit solution of the temperature dependence of the superconducting gap $\Delta(T)$, with $N(0)V = 0.32$ [49–51] and $T_c = 8$ K (see the Supplemental Material [48]). (d) Modulation of transmission and coupling parameters, as a function of the cryostat temperature (normalized by T_c). The measured data (symbols) match our analytical model (lines) based on the coupled-mode formulation with temperature-dependent kinetic inductance.

at 4.75 GHz by biasing the coupler through the isolation port and measuring the coupled and transmitted powers. In Fig. 3(b) we show the change of scattering parameters ΔS with the applied current, in agreement with analytical modeling. The increase of kinetic inductance increases S_{41} and reduces S_{21} at the original equal-coupling frequency, which in turn shifts the 50:50 coupling point to a lower frequency (see the Supplemental Material [48]). This feature provides an additional control to correct for postfabrication discrepancies or to fine tune the coupling operation and bandwidth.

When changing the operating temperature, a much wider variation of the kinetic inductance, and hence of the scattering parameters, can be achieved. In Fig. 3(c) we show the expected theoretical temperature dependence of the kinetic inductance obtained through numerical calculation of the superconducting gap, and the corresponding kinetic inductance $L_k(T) \propto [\Delta(T) \tanh(\Delta(T)/T)]^{-1}$ [51,54], using characteristic values for NbN [50]. We characterize the coupling tunability by varying the base temperature of the cryostat and measuring S_{21} and S_{41} at 4.75 GHz. With this measurement setup, the variation of the temperature modulates the kinetic inductance of both the nanowires. In Fig. 3(d) we show tunability of the parameters with temperature, which is in fair agreement with the model. The observed discrepancies with the theoretical curves are attributed to the uncertainty in the modeling parameters used for the calculation of

$\Delta(T)$. Moreover, as the calculation only includes the coupling section, the impact of other elements of the device (e.g., tapers) is not captured. Note that, when the kinetic inductance is far from the design value, the microwave characteristics of the taper can significantly diverge from the intended behavior.

IV. SUMMARY AND CONCLUSION

The device presented in this work achieves 50:50 forward coupling in a dramatically reduced footprint by exploiting the properties of high-inductance superconducting nanowire transmission lines. The coupling section, as configured here, occupies only $416 \mu\text{m}^2$ and can be integrated as is in high-impedance environment circuits with $Z_0 \approx 1.5 \text{ k}\Omega$. Moreover, as the characteristic impedance depends strongly on the device geometry (Appendix B), the device can be matched to a wide variety of high-impedance environments by redesigning the coupling section's width and length, while keeping a small footprint. As mentioned above, the possibility of performing impedance matching using tapered structures allows one to interface the directional coupler to a lower-impedance environment as well. The total occupied footprint, even including the tapers, is still lower than other conventional normal-conductor coupler designs, such as hybrid, Lange, or parallel lines [34], which require approximately 10 mm^2 . Additional footprint reduction may be achieved

by optimizing the packing of current layouts, or by using a higher effective-index transmission-line architecture [42]. Alternatively, a broadside-coupler architecture might be realized, allowing an increase of the capacitive coupling and a further reduction of the coupling length (see the Supplemental Material [48]).

The model developed to support the design of the device is in agreement with the measured response. The disagreement with the measured data, observed in the magnitude of the scattering parameters, is partially due to backward reflections and to device-level losses that are not accounted for in the system calibration. The effects induced by the use of normal conductors (feed lines and ground plane) or lossy dielectrics can be addressed by redesigning the material stack and adapting the layout. The device model also does not include the power-dependent nonlinear effects that might play an additional role when driving the coupler in the highly nonlinear kinetic-inductance regime. This could contribute to the discrepancies observed when testing the coupler for $t \rightarrow 1$, where t is the reduced temperature. The study of the nonlinearities in high-kinetic-inductance transmission lines is beyond the scope of this paper.

The tunability of the coupling parameters opens up the opportunity for the realization of high-impedance tunable microwave devices. For example, a high-impedance single-pole double-throw nonlinear switch could be realized based on this coupler architecture. Tunability with temperature may become practical if a heater element, normal or superconducting [55,56], is fabricated in close proximity to the coupling section. For quantum computers, the distribution of signals during large-scale integration can suffer from changes in basic operating parameters. This creates challenges for operating tunability features, particularly if driving close to the depairing current or the critical temperature. To avoid interfering with the underlying quantum hardware, the tunability with current could be implemented by fully decoupling the dc and rf through the introduction of on-chip bias-tee components at the input and output of the coupler [16].

We suggest that the directional coupler design proposed in this work may find application in existing superconducting quantum architectures, where the integration of superconducting nanowires, in the form of superinductors, has already been demonstrated [29,30,57]. A high-impedance cryogenic tunable forward coupler could be used for tunable qubit-qubit coupling [58], on-chip integration of readout techniques [59], and on-chip signal processing and multiplexing, drastically reducing the necessary wiring from couplers and splitter on the higher temperature stage to the processor at millikelvin. In the effort to scale the size of single-photon detectors arrays, this device could be used to implement architectures based on frequency-multiplexing readout [60,61]. Moreover, our high-impedance platform might provide a more compact

solution for the integrated circuit designs already using micron-sized coupled superconducting transmission lines [16]. Further development of this nanowire-based technology may lead to the realization of a family of high-kinetic-inductance ultracompact microwave devices that form the basis of a superconducting nanowire monolithic microwave integrated circuit technology.

ACKNOWLEDGMENTS

We thank K. O'Brien, K. Peng, and M. Naghiloo for helpful discussions. We thank E. Toomey, J. Simonaitis, and M. Bionta for critical reading of the manuscript. Support for this work is provided in part by the National Science Foundation Grants No. ECCS-2000743 and No. ECCS-2000778 (UNF), and by the Army Research Office (ARO) under Cooperative Agreement No. W911NF-16-2-0192. The views and conclusions contained in this document are those of the authors and should not be interpreted as representing the official policies, either expressed or implied, of the Army Research Office or the U.S. Government. The U.S. Government is authorized to reproduce and distribute reprints for Government purposes notwithstanding any copyright notation herein. D.Z. is supported by the National Science Scholarship from A*STAR, Singapore, and Harvard Quantum Initiative Postdoctoral Fellowship.

APPENDIX A: ANALYTIC MODEL

In this section we describe the analytical modeling of the nanowire coupler, originally presented in Ref. [36]. It is based on a coupled-mode formalism [33,35] adapted to explicitly include the kinetic contribution to the total line inductance.

We consider here the schematic shown in Fig. 1(b). The inductance per unit length of each line has been separated into two components, $\mathcal{L}_{a,b} = \mathcal{L}_{\text{Fa,Fb}} + \mathcal{L}_{\text{ka,kb}}$, which are the geometric (Faraday) and kinetic inductance contributions, respectively. We denote by \mathcal{M} and \mathcal{E} the per-unit-length mutual inductance and coupling capacitance between the two lines, and by $\mathcal{C}_{a,b}$ the per-unit-length self-capacitances, corrected for the fringing field component [62]. We can write the coupled telegrapher's equations as

$$-\partial_z \begin{bmatrix} i_a \\ i_b \end{bmatrix} = \begin{bmatrix} \mathcal{C}_a + \mathcal{E} & -\mathcal{E} \\ -\mathcal{E} & \mathcal{C}_b + \mathcal{E} \end{bmatrix} \partial_t \begin{bmatrix} v_a \\ v_b \end{bmatrix}, \quad (\text{A1a})$$

$$-\partial_z \begin{bmatrix} v_a \\ v_b \end{bmatrix} = \begin{bmatrix} \mathcal{L}_a + \mathcal{M} & -\mathcal{M} \\ -\mathcal{M} & \mathcal{L}_b + \mathcal{M} \end{bmatrix} \partial_t \begin{bmatrix} i_a \\ i_b \end{bmatrix}. \quad (\text{A1b})$$

Taking the partial derivative with respect to z of Eq. (A1b) and substituting into Eq. (A1a) we have

$$\partial_z^2 \begin{bmatrix} v_a \\ v_b \end{bmatrix} = \begin{bmatrix} \alpha_a & \gamma_a \\ \gamma_b & \alpha_b \end{bmatrix} \partial_t^2 \begin{bmatrix} v_a \\ v_b \end{bmatrix} \quad (\text{A2})$$

with

$$\alpha_a = (\mathcal{L}_a + \mathcal{M})(\mathcal{C}_a + \mathcal{E}) + \mathcal{M}\mathcal{E}, \quad (\text{A3})$$

$$\gamma_a = -\mathcal{E}(\mathcal{L}_a + \mathcal{M}) - \mathcal{M}(\mathcal{C}_b + \mathcal{E}), \quad (\text{A4})$$

$$\alpha_b = (\mathcal{L}_b + \mathcal{M})(\mathcal{C}_b + \mathcal{E}) + \mathcal{E}\mathcal{M}, \quad (\text{A5})$$

$$\gamma_b = -\mathcal{M}(\mathcal{C}_a + \mathcal{E}) - \mathcal{E}(\mathcal{L}_b + \mathcal{M}). \quad (\text{A6})$$

When two transmission lines are brought in close proximity, their coupling produces mode splitting into common (c) and differential (π) modes, having different effective indices and propagation constants. Assuming that the voltages in the two lines $v_{a,b}(z, t)$ propagate in the form of $v_{a,b} = V_{a,b}e^{j\omega t - j\beta z}$ for the eigenmodes, we can solve the dispersion relation

$$\frac{\beta_{c,\pi}^2}{\omega^2} = \frac{\alpha_a + \alpha_b \pm \sqrt{(\alpha_a - \alpha_b)^2 + 4\gamma_a\gamma_b}}{2}, \quad (\text{A7})$$

and, for the two eigenmodes, the voltage ratios on the two lines are

$$R_{c,\pi} = \frac{v_b}{v_a} = \frac{\alpha_b - \alpha_a \pm \sqrt{(\alpha_a - \alpha_b)^2 + 4\gamma_a\gamma_b}}{2\gamma_a}. \quad (\text{A8})$$

We now derive the general solution for the voltages on the lines in terms of forward and backward propagating waves for the c and π modes:

$$V_a(z) = A_1e^{-j\beta cz} + A_2e^{j\beta cz} + A_3e^{-j\beta\pi z} + A_4e^{j\beta\pi z}, \quad (\text{A9})$$

$$V_b(z) = A_1R_c e^{-j\beta cz} + A_2R_c e^{j\beta cz} + A_3R_\pi e^{-j\beta\pi z} + A_4R_\pi e^{j\beta\pi z}. \quad (\text{A10})$$

The currents on the line can be obtained by substituting Eqs. (A9) and (A10) into Eq. (A1b):

$$I_a(z) = \frac{A_1}{Z_{c,a}}e^{-j\beta cz} - \frac{A_2}{Z_{c,a}}e^{j\beta cz} + \frac{A_3}{Z_{\pi,a}}e^{-j\beta\pi z} - \frac{A_4}{Z_{\pi,a}}e^{j\beta\pi z}, \quad (\text{A11})$$

$$I_b(z) = \frac{R_c A_1}{Z_{c,b}}e^{-j\beta cz} - \frac{R_c A_2}{Z_{c,b}}e^{j\beta cz} + \frac{R_\pi A_3}{Z_{\pi,b}}e^{-j\beta\pi z} - \frac{R_\pi A_4}{Z_{\pi,b}}e^{j\beta\pi z}. \quad (\text{A12})$$

Here $Z_{c,a,b}$ and $Z_{\pi,a,b}$ denote the common and differential mode impedances [35], given by

$$Z_{c,a} = \frac{\omega}{\beta_c} \frac{(\mathcal{L}_a + \mathcal{M})(\mathcal{L}_b + \mathcal{M}) - \mathcal{M}^2}{\mathcal{L}_b + \mathcal{M} + \mathcal{M}R_c}, \quad (\text{A13})$$

$$Z_{c,b} = \frac{R_c \omega}{\beta_c} \frac{(\mathcal{L}_a + \mathcal{M})(\mathcal{L}_b + \mathcal{M}) - \mathcal{M}^2}{(\mathcal{L}_a + \mathcal{M})R_c + \mathcal{M}}, \quad (\text{A14})$$

$$Z_{\pi,a} = \frac{\omega}{\beta_\pi} \frac{(\mathcal{L}_a + \mathcal{M})(\mathcal{L}_b + \mathcal{M}) - \mathcal{M}^2}{\mathcal{L}_b + \mathcal{M} + \mathcal{M}R_\pi}, \quad (\text{A15})$$

$$Z_{\pi,b} = \frac{R_\pi \omega}{\beta_c} \frac{(\mathcal{L}_a + \mathcal{M})(\mathcal{L}_b + \mathcal{M}) - \mathcal{M}^2}{(\mathcal{L}_a + \mathcal{M})R_\pi + \mathcal{M}}. \quad (\text{A16})$$

Finally, the port voltages can be evaluated by applying the boundary conditions

$$[V_{\text{in}} - V_a(z = -l)]/Z_{La} = I_a(z = -l), \quad (\text{A17})$$

$$-V_b(z = -l)/Z_{Lb} = I_b(z = -l), \quad (\text{A18})$$

$$V_a(z = 0)/Z_{La} = I_a(z = 0), \quad (\text{A19})$$

$$V_b(z = 0)/Z_{Lb} = I_b(z = 0), \quad (\text{A20})$$

where V_{in} is the input voltage at port 1 and Z_{Lb} and Z_{La} are the load impedances.

For a symmetric coupler, $\mathcal{L}_a = \mathcal{L}_b = \mathcal{L}$ and $\mathcal{C}_a = \mathcal{C}_b = \mathcal{C}$. Moreover, we assume that $\mathcal{M}/\mathcal{L} \ll 1$, and the propagation constants reduce to

$$\beta_c = \omega\sqrt{\mathcal{L}\mathcal{C}}, \quad (\text{A21})$$

$$\begin{aligned} \beta_\pi &= \omega\sqrt{\mathcal{L}\mathcal{C}}\sqrt{1 + \frac{2\mathcal{E}}{\mathcal{C}} + \frac{2\mathcal{M}}{\mathcal{L}} + \frac{4\mathcal{M}\mathcal{E}}{\mathcal{L}\mathcal{C}}} \\ &\approx \omega\sqrt{\mathcal{L}\mathcal{C}}\sqrt{1 + \frac{2\mathcal{E}}{\mathcal{C}}}, \end{aligned} \quad (\text{A22})$$

and, similarly, the impedances for the c and π modes reduce to

$$Z_c = \sqrt{\frac{\mathcal{L}}{\mathcal{C}}}, \quad (\text{A23})$$

$$\begin{aligned} Z_\pi &= \sqrt{\frac{\mathcal{L}}{\mathcal{C}} \frac{\sqrt{1 + 2\mathcal{E}/\mathcal{C} + 2\mathcal{M}/\mathcal{L} + 4\mathcal{M}\mathcal{E}/(\mathcal{L}\mathcal{C})}}{1 + 2\mathcal{E}/\mathcal{C}}} \\ &\approx \sqrt{\frac{\mathcal{L}}{\mathcal{C}}} \frac{1}{\sqrt{1 + 2\mathcal{E}/\mathcal{C}}}. \end{aligned} \quad (\text{A24})$$

A signal injected through the input port is a superposition of the two modes and the energy propagates through the

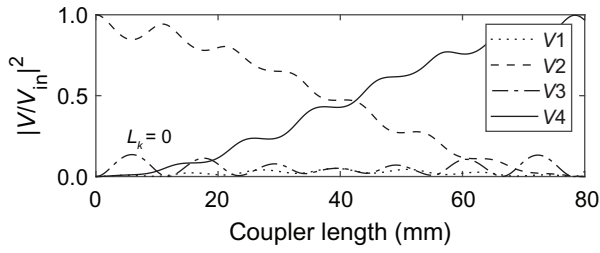


FIG. 4. Analytical calculation of the ports voltage for a coupler section made of normal conductor (lossless with $L_k = 0$). The physical dimensions are the same as in Fig. 1(c).

coupled structures, shuttling between the two lines with a periodicity $l_\pi = \pi/\Delta\beta$. Here

$$\Delta\beta = \beta_\pi - \beta_c \approx \omega\sqrt{\mathcal{L}\mathcal{C}}(\sqrt{1 + \mathcal{E}/\mathcal{C}} - 1). \quad (\text{A25})$$

From Eq. (A25), the minimum length required for 50:50 forward coupling is

$$\frac{l_{\pi,sc}}{2} = \frac{\pi}{2} \frac{1}{\Delta\beta} \approx \frac{\lambda_c}{4} \frac{1}{\sqrt{1 + \mathcal{E}/\mathcal{C}} - 1}, \quad (\text{A26})$$

where λ_c is the guided wavelength for the common mode. Note that in the high-inductance regime, the coupling is mostly determined by the kinetic inductance and the capacitance terms.

The calculation for a symmetric coupling section with a $L_k = 80$ pH per square is shown in Fig. 1(c). In Fig. 4 we show that a side-coupled stripline architecture made of normal conductors can also achieve 50:50 forward coupling, but an approximate 40 mm coupling length is required.

APPENDIX B: NANOWIRE STRIPLINE CHARACTERISTIC IMPEDANCE, PHASE VELOCITY, AND EFFECTIVE INDEX

In Fig. 5, we show the simulation of the characteristic impedance, phase velocity fraction, and effective index of our nanowire stripline. We studied the dependence of these parameters on the width of the nanowire and its kinetic inductance. The material stack is simulated as in the insets of the plots. The top and bottom grounds are simulated as perfect electric conductors (PECs).

APPENDIX C: FABRICATION PROCESS

An approximately 7 nm thick NbN film is sputter deposited [63] on a 2×2 cm² high-resistivity Si substrate. The room-temperature sheet resistance is $R_s = 360$ Ω per square, the residual resistance ratio RRR = 0.8, and the critical temperature $T_C = 8.8$ K.

The sheet kinetic inductance at $T = 0$ K can be estimated as [51] $L_k = (\hbar R_s)/(\text{RRR}\pi\Delta_0) \approx 70.5$ pH per square, where Δ_0 is the zero-temperature superconducting gap. In practice, the base value is tuned by acting on the thickness of the film. Film storage and the fabrication process may induce the degradation of the superconducting properties of the film, resulting in a higher sheet resistance and a lower critical temperature. For a device fabricated with a similar NbN film, we recently reported $L_k \approx 80$ pH per square [42], approximately 10% higher than the theoretical estimation.

We start with the fabrication of 50 Ω coplanar waveguide feed lines using direct writing photolithography (DWL), followed by gold evaporation and liftoff. We pattern the nanowire transmission lines and Klopfenstein tapers by aligned negative-tone electron beam lithography, using ma-N 2401 [64], and we transfer the patterns into the NbN through reactive ion etching with CF₄. We

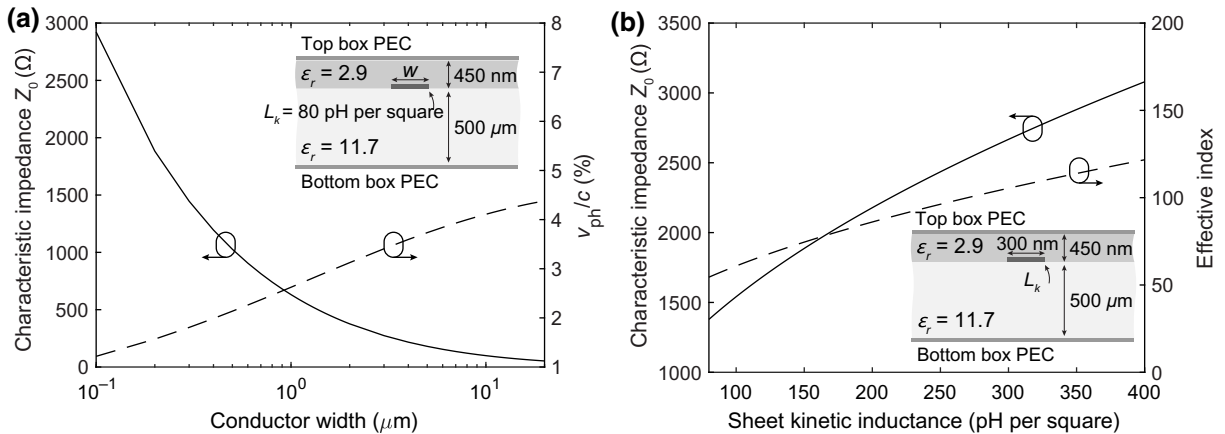


FIG. 5. Simulation of the nanowire stripline parameters. (a) Characteristic impedance and phase velocity fraction versus conductor width for a sheet kinetic inductance $L_k = 80$ pH per square. (b) Characteristic impedance and effective index for a 300 nm wide stripline, as a function of the kinetic inductance.

complete the microstrip structure by patterning a 450 nm hydrogen silsequioxane (FOX-16) dielectric spacer, having $\epsilon_r = 2.9$, using a purposely designed low-contrast electron beam lithography process [39]. Lastly, we fabricate the top ground, with aligned DWL, followed by gold evaporation and liftoff. After fabrication, the width of the lines is 320 nm while physical separation is reduced to 180 nm, due to the proximity effect. The superconducting transition of the fabricated device is observed at $T_c \approx 8$ K, reflecting film degradation during fabrication. Each chip contains four coupler dies and several other test structures. The measurements reported in this paper are all obtained from one device. The micrographs of Fig. 1(a) are from a test structure fabricated with exactly the same process on the same starting wafer. A die designed for 10 GHz is also fabricated and tested, with worse performance due to limitations of the testing setup at higher frequencies. The packaging consisted of a custom made gold-plated copper box with a copper-plated Rogers 4003C PCB.

APPENDIX D: KLOPFENSTEIN IMPEDANCE-MATCHING TAPER

To interface the high-impedance nanowire to the 50 Ω rf electronics, we designed a Klopfenstein impedance-matching taper following the methods of Refs. [41,42,44]. The taper transforms the impedance of a transmission line, minimizing reflections. One end of the taper has a width of 300 nm to match the nanowire transmission line at the coupler section. The other end of the taper is designed to provide a 50 Ω characteristic impedance to match the room-temperature testing electronics. For the microwave environment of this transmission line, 50 Ω is obtained with a width of approximately 15 μm . The taper has a total length of approximately 1.97 mm in 5214 sections, with approximately 1178 squares, for a total inductance of approximately 94 nH, assuming that $L_k = 80$ pH per square. The cutoff frequency is designed to be $f_{co} = 2.5$ GHz. The layout of the taper, as fabricated, is shown in Fig. 1(a)(iii). In Fig. 6 we compare simulation and experimental data for a structure made of two coplanar waveguide feedlines, two impedance-matching tapers, and a straight 520- μm -long nanowire in between. The Klopfenstein taper is affected by an in-band ripple (inset) that conditions the S parameters of the coupler. To minimize this effect, an alternative taper design might be utilized [41,45]. When including the nominal ohmic loss, the experimental data are close to the simulation. As observed in the main text, the characterization of this device shows the same discrepancies as for the four-port coupler. The overall spectrum is shifted to lower frequencies of about 500 MHz, indicating a possible underestimation of the kinetic inductance. Additional amplitude disagreement might be due to insertion loss contributions that are not accounted for in the calibration.

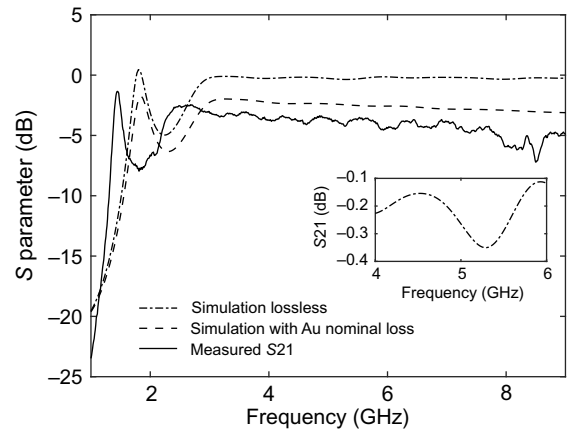


FIG. 6. Transmission simulation and measurement for a structure made of two coplanar waveguide feedlines, two impedance-matching tapers, and a straight 520- μm -long nanowire in between. Inset: in-band ripple.

APPENDIX E: ASYMMETRIC COUPLER FOR EXTENDED BANDWIDTH

Single-section symmetric parallel line couplers provide a relatively narrow bandwidth for 3 dB coupling [40]. When the uncoupled propagation constants are the same (symmetric), the power traveling on one line can be fully transferred to the other line. Effectively, this behavior allows arbitrary coupling ratios, but limits the operation bandwidth for a fixed value, i.e., 50:50 coupling is at a single frequency only.

Wideband operation can be obtained with asymmetric couplers where the two parallel lines have different widths and, therefore, a different uncoupled propagation constant. In this case the maximum power transfer is limited to a

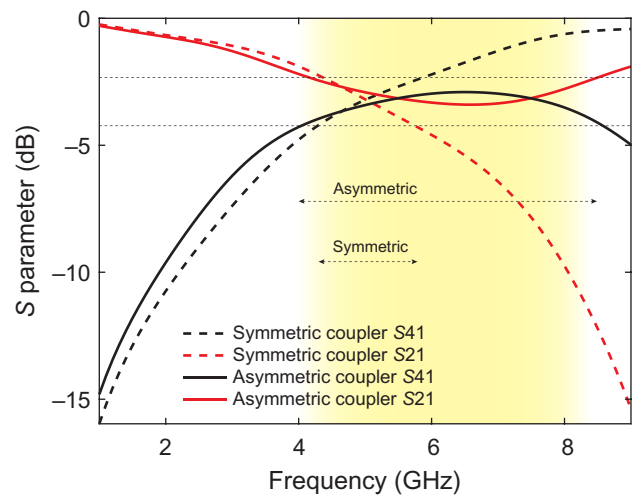


FIG. 7. Transmission and coupling S parameters for symmetric and asymmetric coupler designs. The asymmetric coupler achieves a wider operation bandwidth.

certain portion and one could choose to design the parameters to transfer exactly half of the maximum, effectively extending the operation bandwidth.

We simulated an asymmetric version of our original layout. We set the coupled stripline width (port 3–port 4) to 100 nm while we kept all the other parameters unchanged. In Fig. 7 we show the extended bandwidth achieved with the asymmetric design. The symmetric coupler 10% operation bandwidth is approximately 4.4 to 5.8 GHz. The asymmetric coupler operates between approximately 4 and 8.5 GHz.

-
- [1] A. Blais, S. M. Girvin, and W. D. Oliver, Quantum information processing and quantum optics with circuit quantum electrodynamics, *Nat. Phys.* **16**, 247 (2020).
- [2] F. Arute, K. Arya, R. Babbush, D. Bacon, J. C. Bardin, R. Barends, R. Biswas, S. Boixo, F. G. Brandao, and D. A. Buell *et al.*, Quantum supremacy using a programmable superconducting processor, *Nature* **574**, 505 (2019).
- [3] J. M. Gambetta, J. M. Chow, and M. Steffen, Building logical qubits in a superconducting quantum computing system, *Npj Quantum Inf.* **3**, 1 (2017).
- [4] I. Holzman and Y. Ivry, Superconducting nanowires for single-photon detection: Progress, challenges, and opportunities, *Adv. Quantum Technol.* **2**, 1800058 (2019).
- [5] R. Fagaly, Superconducting quantum interference device instruments and applications, *Rev. Sci. Instrum.* **77**, 101101 (2006).
- [6] M. Buchner, K. Höfler, B. Henne, V. Ney, and A. Ney, Tutorial: Basic principles, limits of Detection, and Pitfalls of Highly Sensitive SQUID Magnetometry for Nanomagnetism and Spintronics, *J. Appl. Phys.* **124**, 161101 (2018).
- [7] J. Zmuidzinas, Superconducting microresonators: Physics and applications, *Annu. Rev. Condens. Matter Phys.* **3**, 169 (2012).
- [8] S. McHugh, B. A. Mazin, B. Serfass, S. Meeker, K. O'Brien, R. Duan, R. Raffanti, and D. Werthimer, A readout for large arrays of microwave kinetic inductance detectors, *Rev. Sci. Instrum.* **83**, 44702 (2012).
- [9] J. C. Bardin *et al.*, in *Dig. Tech. Pap. - IEEE Int. Solid-State Circuits Conf.* (IEEE, San Francisco, CA, 2019), Vol. 2019-February, p. 456.
- [10] B. Patra, R. M. Incandela, J. P. Van Dijk, H. A. Homulle, L. Song, M. Shahmohammadi, R. B. Staszewski, A. Vladimirescu, M. Babaie, F. Sebastiano, and E. Charbon, Cryo-CMOS circuits and systems for quantum computing applications, *IEEE J. Solid-State Circuits* **53**, 309 (2018).
- [11] J. M. Hornibrook, J. I. Colless, I. D. Conway Lamb, S. J. Pauka, H. Lu, A. C. Gossard, J. D. Watson, G. C. Gardner, S. Fallahi, M. J. Manfra, and D. J. Reilly, Cryogenic Control Architecture for Large-Scale Quantum Computing, *Phys. Rev. Appl.* **3**, 24010 (2015).
- [12] P. Borodulin, N. El-Hinnawy, A. L. Graninger, M. R. King, C. R. Padilla, L. N. Upton, R. T. Hinkey, T. E. Schlesinger, A. A. Pesetski, M. E. Sherwin, and R. M. Young, Operation of a latching, low-loss, wideband microwave phase-change switch below 1 K, *J. Low Temp. Phys.* **194**, 273 (2019).
- [13] A. Ruffino, Y. Peng, F. Sebastiano, M. Babaie, and E. Charbon, in *2019 IEEE Radio Frequency Integrated Circuits Symposium (RFIC)* (IEEE, Boston, MA, 2019), p. 107.
- [14] M. Pechal, J. C. Besse, M. Mondal, M. Oppliger, S. Gasparinetti, and A. Wallraff, Superconducting Switch for Fast On-Chip Routing of Quantum Microwave Fields, *Phys. Rev. Appl.* **6**, 24009 (2016).
- [15] H. S. Ku, F. Mallet, L. R. Vale, K. D. Irwin, S. E. Russek, G. C. Hilton, and K. W. Lehnert, Design and testing of superconducting microwave passive components for quantum information processing, *IEEE Trans. Appl. Supercond.* **21**, 452 (2011).
- [16] A. Grimm, F. Blanchet, R. Albert, J. Leppäkangas, S. Jebari, D. Hazra, F. Gustavo, J.-L. Thomassin, E. Dupont-Ferrier, and F. Portier *et al.*, Bright On-Demand Source of Antibunched Microwave Photons Based on Inelastic Cooper Pair Tunneling, *Phys. Rev. X* **9**, 021016 (2019).
- [17] E. Leonard, M. A. Beck, J. Nelson, B. G. Christensen, T. Thorbeck, C. Howington, A. Opremcak, I. V. Pechenezhskiy, K. Dodge, N. P. Dupuis, M. D. Hutchings, J. Ku, F. Schlenker, J. Suttle, C. Wilen, S. Zhu, M. G. Vavilov, B. L. Plourde, and R. McDermott, Digital Coherent Control of a Superconducting Qubit, *Phys. Rev. Appl.* **11**, 14009 (2019).
- [18] G. Brummer, R. Rafique, and T. A. Ohki, Phase and amplitude modulator for microwave pulse generation, *IEEE Trans. Appl. Supercond.* **21**, 583 (2011).
- [19] B. J. Chapman, B. A. Moores, E. I. Rosenthal, J. Kerckhoff, and K. W. Lehnert, General purpose multiplexing device for cryogenic microwave systems, *Appl. Phys. Lett.* **108**, 222602 (2016).
- [20] O. Naaman, J. A. Strong, D. G. Ferguson, J. Egan, N. Bailey, and R. T. Hinkey, Josephson junction microwave modulators for qubit control, *J. Appl. Phys.* **121**, 73904 (2017).
- [21] O. Naaman, M. O. Abutaleb, C. Kirby, and M. Rennie, On-chip josephson junction microwave switch, *Appl. Phys. Lett.* **108**, 112601 (2016).
- [22] B. Abdo, M. Brink, and J. M. Chow, Gyration Operation Using Josephson Mixers, *Phys. Rev. Appl.* **8**, 34009 (2017).
- [23] P. J. Lowell, J. A. Mates, W. B. Doriese, G. C. Hilton, K. M. Morgan, D. S. Swetz, J. N. Ullom, and D. R. Schmidt, A thin-film cryotron suitable for use as an ultra-low-temperature switch, *Appl. Phys. Lett.* **109**, 142601 (2016).
- [24] A. Wagner, L. Ranzani, G. Ribeill, and T. A. Ohki, Demonstration of a superconducting nanowire microwave switch, *Appl. Phys. Lett.* **115**, 172602 (2019).
- [25] N. A. Masluk, I. M. Pop, A. Kamal, Z. K. Mineev, and M. H. Devoret, Microwave Characterization of Josephson Junction Arrays: Implementing a low Loss Superinductance, *Phys. Rev. Lett.* **109**, 137002 (2012).
- [26] P. Groszkowski, A. D. Paolo, A. L. Grimsmo, A. Blais, D. I. Schuster, A. A. Houck, and J. Koch, Coherence properties of the $0-\pi$ qubit, *New J. Phys.* **20**, 43053 (2018).
- [27] M. Kjaergaard, M. E. Schwartz, J. Braumüller, P. Krantz, J. I.-J. Wang, S. Gustavsson, and W. D. Oliver,

- Superconducting qubits: Current state of play, *Annu. Rev. Condens. Matter Phys.* **11**, 369 (2019).
- [28] L. Grünhaupt, M. Spiecker, D. Gusenkova, N. Maleeva, S. T. Skacel, I. Takmakov, F. Valenti, P. Winkel, H. Rotzinger, W. Wernsdorfer, A. V. Ustinov, and I. M. Pop, Granular aluminium as a superconducting material for high-impedance quantum circuits, *Nat. Mater.* **18**, 816 (2019).
- [29] T. M. Hazard, A. Gyenis, A. Di Paolo, A. T. Asfaw, S. A. Lyon, A. Blais, and A. A. Houck, Nanowire Superinductance Fluxonium Qubit, *Phys. Rev. Lett.* **122**, 10504 (2019).
- [30] D. Niepce, J. Burnett, and J. Bylander, High Kinetic Inductance nbn Nanowire Superinductors, *Phys. Rev. Appl.* **11**, 044014 (2019).
- [31] X. Gu, A. F. Kockum, A. Miranowicz, Y. xi Liu, and F. Nori, Microwave photonics with superconducting quantum circuits, *Phys. Rep.* **718-719**, 1 (2017).
- [32] S. Krinner, S. Storz, P. Kurpiers, P. Magnard, J. Heinsoo, R. Keller, J. Lütolf, C. Eichler, and A. Wallraff, Engineering cryogenic setups for 100-qubit scale superconducting circuit systems, *EPJ Quantum Technol.* **6**, 2 (2019).
- [33] G. Ramesh, I. Bahl, and M. Bozzi, *Microstrip lines and slotlines* (Artech house, Boston and London, 2013), p. 433.
- [34] D. M. Pozar, *Microwave Engineering*, 3rd (2005).
- [35] V. K. Tripathi, Asymmetric coupled transmission lines in an inhomogeneous medium, *IEEE Trans. Microwave Theory Tech.* **23**, 734 (1975).
- [36] D. Zhu, Ph.D. thesis, Massachusetts Institute of Technology, 2019.
- [37] M. Morgan and S. Weinreb, in *IEEE MTT-S Int. Microw. Symp. Dig.*, (IEEE, Philadelphia, PA, 2003), Vol. 2, p. 1227.
- [38] G. Maier, *Low dielectric constant polymers for microelectronics* (2001).
- [39] D. Zhu, Q. Y. Zhao, H. Choi, T. J. Lu, A. E. Dane, D. Englund, and K. K. Berggren, A scalable multi-photon coincidence detector based on superconducting nanowires, *Nat. Nanotechnol.* **13**, 596 (2018).
- [40] P. K. Ikkäläinen and G. L. Matthaei, Wideband, forward-coupling microstrip hybrids with high directivity, *IEEE Trans. Microw. Theory Tech.* **35**, 719 (1987).
- [41] R. W. Klopfenstein, A transmission line taper of improved design, *Proc. IRE* **44**, 31 (1956).
- [42] D. Zhu, M. Colangelo, B. A. Korzh, Q. Y. Zhao, S. Frasca, A. E. Dane, A. E. Velasco, A. D. Beyer, J. P. Allmaras, E. Ramirez, W. J. Strickland, D. F. Santavicca, M. D. Shaw, and K. K. Berggren, Superconducting nanowire single-photon detector with integrated impedance-matching taper, *Appl. Phys. Lett.* **114**, 42601 (2019).
- [43] Q. Y. Zhao, D. Zhu, N. Celandri, A. E. Dane, A. N. McCaughan, F. Bellei, H. Z. Wang, D. F. Santavicca, and K. K. Berggren, Single-photon imager based on a superconducting nanowire delay line, *Nat. Photonics* **11**, 247 (2017).
- [44] D. Zhu, M. Colangelo, C. Chen, B. A. Korzh, F. N. Wong, M. D. Shaw, and K. K. Berggren, Resolving photon numbers using a superconducting nanowire with impedance-matching taper, *Nano Lett.* **20**, 3858 (2020).
- [45] R. P. Erickson, Variational theory of the tapered impedance transformer, *J. Appl. Phys.* **123**, 074501 (2018).
- [46] S. Miller, Coupled wave theory and waveguide applications, *Bell Syst. Tech. J.* **33**, 661 (1954).
- [47] D. M. Pozar, *Microwave Engineering* (John Wiley & Sons Inc, 2011), p. 317.
- [48] See Supplemental Material at <http://link.aps.org/supplemental/10.1103/PhysRevApplied.15.024064> for additional details on microwave simulations, design, and measurement setup.
- [49] L. Kang, B. Jin, X. Liu, X. Jia, J. Chen, Z. Ji, W. Xu, P. Wu, S. Mi, and A. Pimenov *et al.*, Suppression of superconductivity in epitaxial nbn ultrathin films, *J. Appl. Phys.* **109**, 033908 (2011).
- [50] T. Polakovic, S. Lendinez, J. E. Pearson, A. Hoffmann, V. Yefremenko, C. L. Chang, W. Armstrong, K. Hafidi, G. Karapetrov, and V. Novosad, Room temperature deposition of superconducting niobium nitride films by ion beam assisted sputtering, *APL Mater.* **6**, 76107 (2018).
- [51] M. Tinkham, *Introduction to Superconductivity* (Courier Corporation, Dover Publications. Mineola, New York, 2004), p. 43.
- [52] J. R. Clem and V. G. Kogan, Kinetic impedance and depairing in thin and narrow superconducting films, *Phys. Rev. B - Condens. Matter Mater. Phys.* **86**, 174521 (2012).
- [53] S. Frasca, B. Korzh, M. Colangelo, D. Zhu, A. E. Lita, J. P. Allmaras, E. E. Wollman, V. B. Verma, A. E. Dane, E. Ramirez, A. D. Beyer, S. W. Nam, A. G. Kozorezov, M. D. Shaw, and K. K. Berggren, Determining the depairing current in superconducting nanowire single-photon detectors, *Phys. Rev. B* **100**, 54520 (2019).
- [54] D. F. Santavicca, J. K. Adams, L. E. Grant, A. N. McCaughan, and K. K. Berggren, Microwave dynamics of high aspect ratio superconducting nanowires studied using self-resonance, *J. Appl. Phys.* **119**, 234302 (2016).
- [55] R. Baghdadi, J. P. Allmaras, B. A. Butters, A. E. Dane, S. Iqbal, A. N. McCaughan, E. A. Toomey, Q.-Y. Zhao, A. G. Kozorezov, and K. K. Berggren, Multilayered Heater Nanocryotron: A Superconducting-Nanowire-Based Thermal Switch, *Phys. Rev. Appl.* **14**, 054011 (2020).
- [56] A. N. McCaughan, V. B. Verma, S. M. Buckley, J. Allmaras, A. Kozorezov, A. Tait, S. Nam, and J. Shainline, A superconducting thermal switch with ultrahigh impedance for interfacing superconductors to semiconductors, *Nat. Electron.* **2**, 451 (2019).
- [57] J. Ku, V. Manucharyan, and A. Bezryadin, Superconducting nanowires as nonlinear inductive elements for qubits, *Phys. Rev. B* **82**, 134518 (2010).
- [58] P. Krantz, M. Kjaergaard, F. Yan, T. P. Orlando, S. Gustavsson, and W. D. Oliver, A quantum engineer's guide to superconducting qubits, *Appl. Phys. Rev.* **6**, 21318 (2019).
- [59] B. Abdo, N. T. Bronn, O. Jinka, S. Olivadese, A. D. Córcoles, V. P. Adiga, M. Brink, R. E. Lake, X. Wu, D. P. Pappas, and J. M. Chow, Active protection of a

- superconducting qubit with an interferometric josephson isolator, *Nat. Commun.* **10**, 1 (2019).
- [60] S. Doerner, A. Kuzmin, S. Wuensch, I. Charaev, F. Boes, T. Zwick, and M. Siegel, Frequency-multiplexed bias and readout of a 16-pixel superconducting nanowire single-photon detector array, *Appl. Phys. Lett.* **111**, 32603 (2017).
- [61] A. K. Sinclair, E. Schroeder, D. Zhu, M. Colangelo, J. Glasby, P. D. Mauskopf, H. Mani, and K. K. Berggren, Demonstration of microwave multiplexed readout of DC-biased superconducting nanowire detectors, *IEEE Trans. Appl. Supercond.* **29**, 1 (2019).
- [62] S. S. Bedair, Characteristics of some asymmetrical coupled transmission lines, *IEEE Trans. Microw. Theory Tech.* **32**, 108 (1984).
- [63] A. E. Dane, A. N. McCaughan, D. Zhu, Q. Zhao, C. S. Kim, N. Calandri, A. Agarwal, F. Bellei, and K. K. Berggren, Bias sputtered NbN and superconducting nanowire devices, *Appl. Phys. Lett.* **111**, 122601 (2017).
- [64] E. Toomey, M. Colangelo, and K. K. Berggren, Investigation of ma-N 2400 series photoresist as an electron-beam resist for superconducting nanoscale devices, *J. Vac. Sci. Technol. B* **37**, 051207 (2019).